A&A 676, A29 (2023)
https://doi.org/10.1051/0004-6361/202346320

Astronomy & Astrophysics

VLBI imaging of high-redshift galaxies and protoclusters at low radio frequencies with the International LOFAR Telescope

C. M. Cordun[1], R. Timmerman[1], G. K. Miley[1], R. J. van Weeren[1], F. Sweijen[1,2], L. K. Morabito[3,4], and H. J. A. Röttgering[1]

[1] Leiden Observatory, Leiden University, PO Box 9513, 2300 RA Leiden, The Netherlands
e-mail: c.m.cordun@umail.leidenuniv.nl
[2] ASTRON, Netherlands Institute for Radio Astronomy, Oude Hoogeveensedijk 4, 7991 PD Dwingeloo, The Netherlands
[3] Centre for Extragalactic Astronomy, Department of Physics, Durham University, Durham DH1 3LE, UK
[4] Institute for Computational Cosmology, Department of Physics, University of Durham, South Road, Durham DH1 3LE, UK

Received 4 March 2023 / Accepted 30 May 2023

ABSTRACT

It is generally known that luminous, ultra-steep spectrum radio sources are preferentially associated with massive galaxies at high redshifts. In this paper, we describe a pilot project directed at such objects to demonstrate the feasibility and importance of using the LOw-Frequency ARray (LOFAR) data to study the most distant massive galaxies undergoing formation and protoclusters. We successfully imaged four high-redshift ($z > 2$), high-luminosity radio galaxies with sub-arcsecond resolution, at 144 MHz, using the International LOFAR Telescope (ILT). Our targets were 4C 41.17, which we dubbed "the Anthill" galaxy ($z = 3.8$), as well as B2 0902+34 ($z = 3.4$), 4C 34.34 ($z = 2.4$), and 4C 43.15 ($z = 2.5$). We mapped their low-frequency morphologies and the spatial distributions of their low-frequency spectral indices and then compared these results with the available optical, infrared, and X-ray images. Both for the Anthill at $z = 3.8$ and B2 0902+34 at $z = 3.4$, the location of the steepest radio emission coincides with the Lyα–emitting ionized gas halo. Our pilot project demonstrates that thanks to its outstanding sensitivity and high angular resolution at low frequencies, the ILT is a unique facility for studying the co-evolution and interaction of massive galaxies, galaxy clusters, and supermassive black holes in the early Universe.

Key words. galaxies: clusters: general – galaxies: high-redshift – radio continuum: galaxies – galaxies: jets – galaxies: nuclei – galaxies: starburst

1. Introduction

High-redshift radio galaxies (HzRG) are among the largest, most luminous, and most massive galaxies in the early Universe (Chambers et al. 1988; Miley & Chambers 1989; McCarthy 1993; Blundell & Rawlings 1999; Miley & De Breuck 2008; Miley et al. 2009; Saxena et al. 2019). They are likely progenitors of massive elliptical and type cD galaxies located at the centers of low-redshift galaxy clusters (Fall & Rees 1977). They can therefore serve as unique laboratories for studying the formation of massive galaxies, protoclusters, and active galactic nuclei (AGNs) as well as their interactions with the surrounding environment.

It was recently suggested that the emergence of massive galaxies, protoclusters, and supermassive black holes is interconnected (Ricarte et al. 2019). Observational evidence for the co-evolution of these three inhabitants of the early Universe includes alignments that have been observed between their radio jets and the associated optical continuum, line-emitting ionized gas, molecular gas, and X-ray emission (Miley & De Breuck 2008). In several cases, the alignments indicate that star formation in the protocluster is triggered by the interaction of the radio-emitting jet with the surrounding intergalactic medium (De Young 1989; Bicknell et al. 2000; Nesvadba et al. 2006). Well-known cases of such alignments include the spectacular "Spiderweb" radio protocluster at $z = 2.2$ (Miley & De Breuck 2008) and the 4C 41.17 radio galaxy at $z = 3.8$. Because of the similarity of 4C 41.17 with the Spiderweb, we have dubbed it the "Anthill" galaxy cluster. Recently, an overdensity of X-ray AGN was detected in the field of the Spiderweb that is an order of magnitude greater than that of the field (Tozzi et al. 2022), implying that this forming protocluster is populated with fast-growing super-massive black holes (SMBHs) and that the early evolution of protoclusters, their central massive galaxies and the associated super-massive black holes (SMBHs) are closely connected. Although distant protoclusters have been detected with other methods (e.g., da Costa & Menéndez-Delmestre 2021; Casey et al. 2015; Adam et al. 2015; Toshikawa et al. 2018; Uchiyama et al. 2022), surveys at low radio frequencies still make up one of the most powerful tools for finding them (Wylezalek et al. 2013) and studying the role of AGNs and SMBHs in their formation and evolution.

One specific characteristic of HzRGs that enables them to be more easily identified in the radio band is the correlation between their spectral index (α) and redshift (z), namely: the $\alpha \sim z$ relation (Tielens et al. 1979). This empirical law indicates that the steeper the overall spectrum is (from low, MHz frequencies to high, GHz frequencies), the higher its redshift is likely to be (Chambers et al. 1990). Hence, ultra-steep spectrum (USS) radio sources pinpoint the most massive galaxies at the largest redshifts. The origin of the $\alpha \sim z$ relation is still not fully understood. One possibility is that the steeper spectral index is due to increased confinement of the radio

lobes by the denser protocluster environment at higher redshifts. This could cause the radio surface brightness of the lobes to remain relatively high, resulting in increased spectral steepening due to energy losses (Klamer et al. 2006). A second explanation is that it originates from a K-correction effect coupled with the concave radio spectra of HzRGs. It has been suggested that about 50% of the $\alpha \sim z$ relation gradient can be explained by such an effect (Ker et al. 2012). A third explanation is that the steeper radio spectrum at higher redshift may be related to increased inverse Compton losses due to upscattering of the cosmic microwave background (CMB) photons by the radio synchrotron-emitting relativistic electrons. We note that the CMB energy density increases as $(1+z)^4$ (e.g., Carilli et al. 2022). A study by Morabito & Harwood (2018) found that inverse Compton losses in flux density limited surveys are enough to reproduce the observed $\alpha \sim z$ relation. Evidence that inverse Compton X-ray radiation of the surrounding environment is directly related to the steep radio spectra has also been found in multiple studies (e.g., Jimenez-Gallardo et al. 2021).

Further investigation of the poorly understood processes that play a role in building massive galaxies, protoclusters, and supermassive black holes (SMBHs) are fundamentally important. In particular, for investigating the interaction of radio jets produced by the nuclear SMBHs of massive central galaxies with other protocluster constituents, it is essential to make high-resolution maps of their radio intensities and spectra at low frequencies. This is the main goal of this study.

The International Low Frequency Telescope (ILT; van Haarlem et al. 2013), with its pan-European baselines is capable of achieving sub-arcsecond resolution in its HBA mode (120–168 MHz). This is an unprecedentedly high spatial resolution at such low frequencies. Because HzRGs (i) usually have steep spectra ($\alpha < -0.9$) and (ii) have an angular size distribution peaked at ∼7″, with 80% of known HzRGs having angular sizes between 5″ and 20″ (Carilli et al. 1997), the ILT is uniquely equipped for detecting and mapping HzRGs.

Making images at the full resolution of the LOw-Frequency ARray (LOFAR) is challenging. The ILT is an interferometric array, with ∼40 000 small antennas concentrated in 52 stations, 38 of them in the Netherlands, 6 in Germany, 3 in Poland, and single stations in France, Great Britain, Ireland, Latvia, and Sweden. The total effective collecting area is ∼300 000 m^2 and the ILT baselines extend beyond ∼2000 km. The stations are connected by fiber optical cables. In its HBA mode, their digitized signals are distributed over 16 frequency channels in each of 240 bands = 3840 frequency channels between 120 and 168 MHz and combined via a supercomputer at the University of Groningen. The continuously changing ionospheric perturbations at low frequencies and the large number of ILT baselines and frequency channels result in huge datasets that need to be calibrated and analyzed (Morabito et al. 2022).

Here, we describe a pilot project to investigate the feasibility of carrying out sub-arcsecond radio imaging at 144 MHz with the ILT of a small sample of HzRGs, using the images to make high-resolution radio spectral distribution studies and comparing these with maps at non-radio wavelengths. The eventual goal is to investigate the interaction of radio jets with the other constituents of forming galaxies and protoclusters and its importance with respect to galaxy and cluster evolution. Our pilot study is based on observations of three targets covered by the LOFAR Two-meter Sky Survey (LoTSS; Shimwell et al. 2019), supplemented by a fourth HzRG target, 4C 43.15 at $z = 2.5$, that has already been mapped at sub-arcsecond resolution using the ILT by Sweijen et al. (2022). Our intention is to eventually extend this pilot study to a larger sample.

Throughout this paper, we assume a ΛCDM cosmology, with the following cosmological parameters: $H_0 = 70\,\mathrm{km\,s^{-1}\,Mpc^{-1}}$, $\Omega_\mathrm{m} = 0.3$, and $\Omega_\Lambda = 0.7$, where H_0 is the Hubble parameter, Ω_m, the matter density parameter, and Ω_Λ, the dark energy density parameter. Moreover, all the images are made using the J2000 coordinate system and we define the spectral index as $S \propto \upsilon^\alpha$, where S is the flux density and υ is the frequency. We refer to spectra that have $\alpha < -1$ as "ultra-steep" (USS).

2. HzRG targets

All of our targets were selected to have archival measurements at higher frequencies with the Very Large Array (VLA), allowing ILT-VLA spectral index distributions to be mapped. These targets are listed in Table 1.

4C 41.17 (i.e., the Anthill radio source) is associated with a spectacular massive galaxy at a redshift of $z = 3.8$ (Miley & De Breuck 2008). It was discovered thanks to its high radio luminosity and ultra-steep spectral index by Chambers et al. (1990). Deep imaging with the HST revealed that the host galaxy is a spectacularly large clumpy group of faint galaxies that appear to be merging with the massive host galaxy. The HST observations provided important early evidence favoring hierarchical galaxy formation models.

Based on several of its properties, the Anthill closely resembles the well-studied Spiderweb Galaxy and protocluster at $z = 2.2$ (Miley & De Breuck 2008). Both are among the most massive, clumpiest, and largest galaxies known, consistent with type cD galaxies in the process of formation. Both are surrounded by giant Lya-emitting ionized halos whose sizes exceed 100 kpc. Furthermore, both the Spiderweb (Di Mascolo et al. 2023) and the Anthill (Emonts et al. 2023) are connected with large gas streams, extending by >100 kpc. Spectroscopically confirmed protocluster-sized galaxy overdensities have been detected around the Spiderweb and several other similar high-luminosity radio galaxies (e.g., Venemans et al. 2007; Tozzi et al. 2022). In the case of the Anthill, no protocluster-sized galaxy overdensity has yet been confirmed (Ivison et al. 2000; Greve et al. 2007; Wylezalek et al. 2013) and there are no *Chandra* X-ray observations of comparable depth to those of the Spiderweb (Tozzi et al. 2022). The fact that the Anthill is a "twin" of the Spiderweb in so many ways offers evidence that it is also the brightest cluster galaxy in the process of formation. However, the associated protocluster galaxies have not yet been detected.

B2 0902+34 has a redshift of $z = 3.4$, a relatively flat optical spectral energy distribution, and it has been suggested to be a protogalaxy undergoing its first episode of star formation (Lilly 1988; Eales et al. 1993; Pentericci et al. 1999). The radio and optical structure of this galaxy has been described as "bizarre", with a flat-spectrum radio core located in a "valley" between 2 optical peaks (Carilli 1995). This HzRG is also exceptional in that it is one of the only $z > 2$ radio sources that has been observed to have an associated narrow HI absorption line (Uson et al. 1991; Chandra et al. 2004).

4C 34.34 has a redshift of $z = 2.4$. It has been mapped with the VLA at higher frequencies (Law-Green et al. 1995) and it is therefore a suitable target for low-frequency spectral index mapping with the ILT observation. However, besides its optical spectrum and a *Spitzer* observation which places it in a highly dense environment (Wylezalek et al. 2013), there are no other optical, infrared, or X-ray data available for this source.

Table 1. Targets selected for 144 MHz sub-arcsecond mapping with the ILT, with properties taken from Miley & De Breuck (2008), ILT project details for each target, and properties of the resultant ILT images.

Object	4C 41.17 (Anthill)	B2 0902+34	4C 34.34	4C 43.15
RA (J2000)	06h50m51.2s	09h05m30.1s	11h16m30.4s	07h35m22.5s
Dec (J2000)	+41°30′31″	+34°07′57″	+34°42′24″	+43°44′25″
Redshift	3.792	3.395	2.400	2.429
Integrated spectral index $\alpha_{144\,\mathrm{MHz}}^{1.4\,\mathrm{GHz}}$	−1.30	−0.93	−0.93	−1.10
Angular size at 144 MHz (arcseconds)	14.3″	11.5″	17.3″	12.3″
Linear size (kpc)	192	150	230	163
Project code	LC6_021 [(2)]	LT10_010 [(1)]	LT10_010 [(2)]	LT5_006 [(2)]
SAS Id	558416	657262	746346	427100
Number of available international stations	50	48	50	47
ILT resolution (arcseconds)	0.2″ × 0.2″	0.4″ × 0.2″	0.3″ × 0.2″	0.4″ × 0.4″
RMS noise level (μJy beam^{-1})	180	134	204	170

Notes. [(1)]LoTSS archive (Shimwell et al. 2017). [(2)]Dedicated project additional to LoTSS.

4C 43.15 has had high-resolution LOFAR ILT maps published, both with the HBA (Sweijen et al. 2022) and the LBA (Morabito et al. 2016). It has a redshift of $z = 2.4$, a bright Lyα halo (Villar-Martín et al. 2003; Motohara et al. 2000), and it is located in a dense region, but with a lower overdensity than most HzRGs (Wylezalek et al. 2013).

3. Data reduction

3.1. Producing sub-arcsecond Images from the ILT

Details of the ILT observations are summarized in Table 1. Each target was observed for a total of eight hours in a frequency band between 120 MHz and 168 MHz. We shall henceforth refer to these data by their central frequency as "144 MHz" data. In addition, a ten-minute long observation of the standard calibration source (3C 295) was taken before and after every target observation.

Making images with the full resolution of ILT is complex and computer-intensive. Unlike the case of most other radio telescopes, LOFAR is a dipole array with a wide field of view and includes a large number of baselines at low frequencies, thus, the data volume is extremely large. The ILT data reduction involves three main steps (Sweijen et al. 2022; Morabito et al. 2022). First, the target and its calibrator need to be processed. During this stage, the phase effects due to clock drifts are separated from those due to the ionosphere (Van Weeren et al. 2016, 2021). Secondly, the data must be processed through the ILT long baseline pipeline to calibrate the international stations. Thirdly, high-resolution images are produced using a self-calibration procedure.

The first stage of the reduction made use of the PREFACTOR software package (Van Weeren et al. 2016; Williams et al. 2016; De Gasperin et al. 2019) to remove instrumental effects and minimize radio-frequency interference (RFI) by flagging the data using the AOFLAGGER package (Offringa et al. 2013, 2015). More specifically, based on the geometry of the array and by comparing our data to a model of the calibration source, we derived corrections for the polarization alignment, the Faraday rotation, the sensitivity as a function of frequency within the bandpass, and clock offsets between the stations. After applying these corrections, the remaining low-level RFI was flagged. Finally, phase corrections for the short-baseline (Dutch) stations were derived from a sky model obtained from the Tata Institute of Fundamental Research (TIFR), namely, the Giant Metrewave Radio Telescope (GMRT) Sky Survey (TGSS, Intema et al. 2017). This calibrated data was averaged to 8 s per integration with frequency channels of 98 kHz.

The second stage involved extending the calibration from the Dutch stations to the pan-European ILT, using the LOFAR-VLBI pipeline (Morabito et al. 2022). The calibration solutions previously derived based on the calibrator source were also applied to the long-baseline ILT data. Then, for each observation, a bright unresolved source from the Long-Baseline Calibrator Survey (LBCS, Jackson et al. 2016, 2022) was used to derive fast phase and slow complex gain calibration solutions, so as to correct as much as possible for perturbations to the wavefronts primarily caused by the ionosphere.

The third stage of the reduction focused on self calibration, using the procedure developed in Van Weeren et al. (2021). In all three of the newly analysed sources, the target was known to possess sufficiently bright compact structure to act as an in-field calibrator based on the Long-Baseline Calibrator Survey (LBCS, Jackson et al. 2016, 2022). Because the core stations had already been calibrated, these could be phased-up to narrow the effective field of view, thereby minimizing the distorting influence on the images from nearby radio sources. The starting model for the self-calibration was derived from the VLA image of the relevant target, (see Sect. 3.2). To derive the optimum set of calibration solutions, we iterated with multiple cycles of self-calibration. In each cycle, we imaged and cleaned the target field using WSClean (Offringa & McKinley 2014; Offringa & Smirnov 2017) and used the deconvolved image as an updated model to derive improved calibration solutions, with the weighting parameters selected to give the best compromise between sensitivity and resolution (e.g., Briggs 1995).

The final angular resolution achieved at 144 MHz was ∼0.3″ (FWHM) for all four targets, the FWHM of the primary beam was ∼2 arcmin, and the maximum recoverable scale is ∼50 arcseconds. An overview of the image properties and noise levels obtained is given in Table 1.

3.2. Complementary VLA images and low-frequency spectral index maps

To produce maps of spectral indices and starting models for the previously discussed self calibration stage of the ILT imaging, we used complementary data at higher frequencies from the Very Large Array (VLA) archive, as summarized in Table 2. The array

Table 2. Complementary VLA observations used in this project.

Object	4C 41.17	B2 0902+34	4C 34.34	4C 41.15
Project code	AM0205, AC0234, AC0316, AI0108, AM 107, AM 0189	AV0157, AB0511, AC0316	AV0157, AR0287	AK410
Observing time (h)				
L band	A config. – 8.4	A config. – 2.1	A config. – 0.5	–
C band	A config. – 2.1	A config. – 2.7	A config. – 0.5	–
	B config. – 0.3	B config. – 0.5	B config. – 1.3	–
U band	B config. – 1.6	–	–	–
	C config. – 0.6	–	–	–
X band	–	–	–	A config – 0.7
Resolution				
L band	1.2″ × 1.0″	1.1″ × 1.0″	1.3″ × 1.1″	-
C band	0.4″ × 0.4″	0.5″ × 0.4″	0.6″ × 0.5″	–
U band	0.4″ × 0.3″	–	–	–
X band	–	–	–	1.05″ × 0.83″

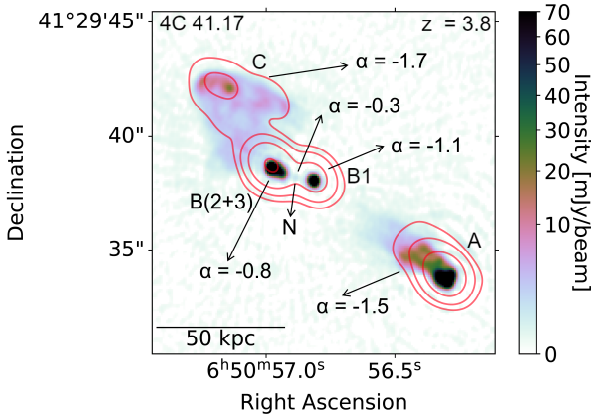

Fig. 1. ILT HBA 144 MHz final processed image of the Anthill at z = 3.8, with a resolution of 0.2″ and the VLA contours in *L* band.

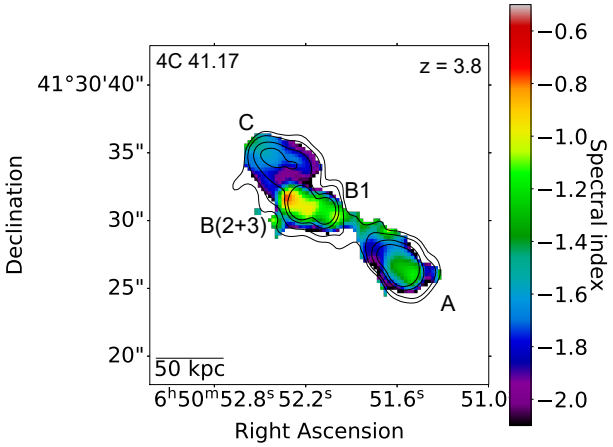

Fig. 2. Map of the low-frequency 144 MHz – 1.4 GHz spectral index of the Anthill at z = 3.8 obtained using the ILT HBA and VLA *L*-band observations. The ILT HBA contours from the smoothed 144 MHz image in Fig. 1 are also displayed on the spectral index map.

configurations were selected to optimally match the ILT angular resolutions. The VLA observations generally consisted of a single scan on a primary calibrator for flux scale and bandpass calibration and multiple short scans on a secondary calibrator between target observations for phase referencing.

The reduction and calibration of the VLA data was carried out using the Common Astronomy Software Application (CASA; McMullin et al. 2007). First, the TFCROP algorithm was used to detect and flag RFI. Calibration tables were then applied to correct for antenna position offsets and gain elevation curves. Next, the primary calibrator was used to set the absolute flux scale, and the secondary calibrator was applied to derive phase corrections for predominantly tropospheric perturbations. These were interpolated to the target scans and applied to the data together with the previously derived calibration tables.

Then, the target data were self-calibrated using WSClean (Offringa & McKinley 2014) for imaging and cleaning, and CASA for deriving updated calibration tables. The self-calibration process initially only derived updated phase calibration tables. When these converged, the self-calibration switched to deriving both phase and amplitude corrections. The PyBDSF software (Mohan & Rafferty 2015) was applied to the final VLA images to derive starting models for the ILT self-calibration.

The final angular resolution achieved was ∼1.2″ (FWHM) at 1.4 GHz (*L* band), ∼0.5″ (FWHM) at 6 GHz (*C* band), ∼0.9″ (FWHM) at 10 GHz (*X* band), and ∼0.4″ (FWHM) at 15 GHz (*U* band), for all four targets. An overview of the image properties is given in Table 2.

The VLA and ILT images were convolved to similar angular resolutions using CASA and aligned with the FITS_TOOLS Python library. Then, low-frequency spectral index maps of each targeted source were made using these images. All pixels whose significance was smaller than 3σ have been flagged.

4. Results

Our results are presented and discussed separately for each of our four targets. We provide images of the high-resolution 144 MHz ILT emission, along with the 144–1420 MHz spectral index maps and (when available) the superpositions of the radio data on optical and X-ray images.

4.1. 4C 41.17 (the Anthill) at z = 3.8

The high-resolution image of the Anthill at 144 MHz is shown in Fig. 1 and its low-frequency spectral index map in Fig. 2, while Fig. 3 shows an overlay of the ILT radio map on the HST optical continuum image (Miley et al. 1992) together with Keck Lyα contours (green, top) and *Chandra* X-ray contours (blue, bottom).

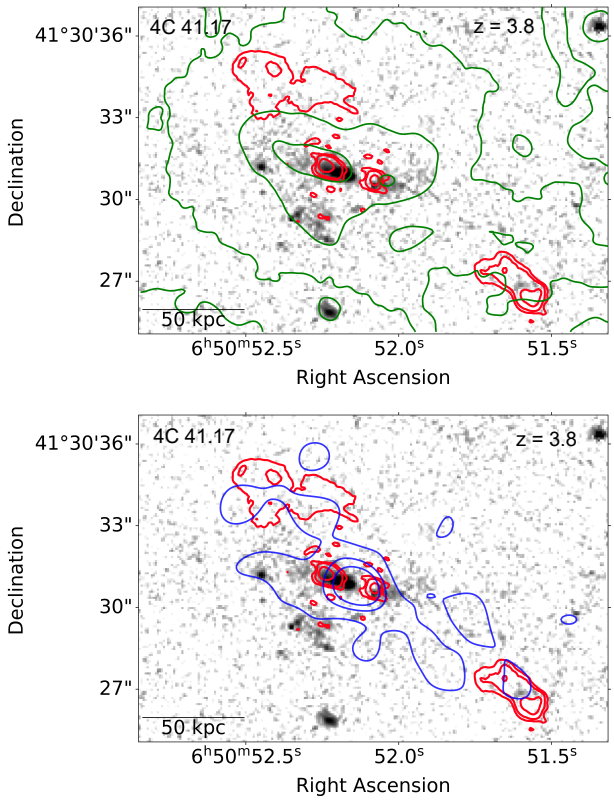

Fig. 3. Overlay of ILT 144 MHz radio image for 4C 41.17 at $z = 3.8$ (red contours) above 3σ noise, superimposed on the HST continuum image (4 h exposure through the *F*702*W* filter of WFPC2 Bicknell et al. 2000). The green contours (top panel) add the Keck Lyα distribution observed by Keck (Reuland et al. 2003), and the blue contours (bottom panel) represent the X-ray distribution observed by *Chandra* (Scharf et al. 2003).

The figures illustrate that the Anthill has several interesting features. First, we note that the individual radio components designated at higher frequencies as A, B1, and C by Chambers et al. (1990), as well as the nucleus (N) detected by Carilli et al. (1994), are distinguishable on our 144 MHz ILT map. However, B2 and B3 are blended at the ILT resolution, so we refer to them as B(2+3). The radio source has an edge-brightened FR-II morphology similar to Cygnus A, with a pair of hot spots at its eastern edge (component C) and a brighter hot spot with a symmetric double narrow feature close to its western edge (component A). There are double features on both sides of the source. This is apparent in the outer pair of eastern hot spots and the bifurcated backward jet-like structure in the western hot spot. This may be coincidental or could be a consequence of their production in the same episode of enhanced nuclear activity. The two pairs of jets could be produced in different activity episodes, with the jet angle between them corresponding to the precession of the radio source (Blundell & Rawlings 1999). However, we suggest that the complex shape of the source is more likely due to interaction between the radio jets and the gaseous halo around the host galaxy, which is commonly observed to occur in HzRGs (Bicknell et al. 2000).

Although the integrated low-frequency spectral index of the Anthill is ultra-steep with $\alpha = -1.2$, there are substantial differences in spectra between the components. The outer components are steepest, with C having $\alpha = -1.60 \pm 0.04$ and A having $\alpha = -1.40 \pm 0.04$. The central compact component (B1) has a spectral index of $\alpha = -1.10 \pm 0.04$, while the offset component, B(2+3), features a flatter spectral index of $\alpha = -0.80 \pm 0.04$. Finally, we detect a faint 1.2 mJy brightness peak at the position of component N, which was previously detected by Chambers et al. (1990) and Carilli et al. (1994). This implies a spectral index of $\alpha \sim -0.3$ between our 144 MHz measurement and the flux density at 4.7 GHz, as reported by Carilli et al. (1994).

Components B1 and B(2+3) are associated with a complex of objects in the optical image that are consistent with merging galaxies in the process of building a massive CD galaxy at the center of the cluster. Their optical emission is likely to be due to some combination of AGN and star formation processes.

An intriguing question is related the nature of component B(2+3). Although it is only slightly resolved on the ILT image, it is resolved into two components on the VLA map. B(2+3) is not aligned with the main collimated radio source structure (A, B1, C) and is co-located with an optical galaxy close to the massive central one. We note that the Anthill is a radio galaxy in which the forming central massive protogalaxy appears to be growing due to merging with several surrounding galaxies. B(2+3) may therefore be fully associated with a second radio galaxy in the cluster that is merging with the central cD protogalaxy responsible for producing the main aligned (A, B1, C) radio source (Gurvits et al. 1997). If the galaxy associated with B(2+3) is indeed merging with the central A, B1, C galaxy the fact that the radio jets (and SMBHs) in both galaxies are oriented in the same direction would be yet another observed alignment in orientation that could have fundamental implications for the origin and growth of SMBHs.

As described by Miley & De Breuck (2008), the HST optical image shows that a group of several galaxies is associated with the 4C 41.17 radio source, indicating that the Anthill is at the center of a rich galaxy cluster that is in the process of building a massive cD galaxy at its center. The whole complex is surrounded by a giant extended Lyα halo and an extended region of X-ray emission. The radio source, cluster galaxies, Lyα emission, and X-ray emission are all approximately aligned with each other, similarly to the case of the Spiderweb radio protocluster (Carilli et al. 2022). The alignments indicate that there is ongoing interaction between the formation of the galaxy group and possible cluster and that the direction of the jets produced by the supermassive black holes associated with the jets is in some way connected with the large-scale formation processes. In particular, the alignment between radio jets and optical components, as well as the complex shape of the source, are indications of strong interactions between the jets and the surrounding gaseous halo, causing jet-induced star formation (Dey et al. 1997; Bicknell et al. 2000).

The correspondence of the low-frequency radio emission and the X-ray images (Scharf et al. 2003) is consistent with the X-ray emission being dominated by inverse Compton up-scattering of the cosmic microwave background photons by the radio-emitting relativistic electrons. This is also similar to the case of the Spiderweb radio protocluster (Carilli et al. 2022).

4.2. B2 0902+34 at $z = 3.4$

The high-resolution image of B2 0902+34 at 144 MHz is shown in Fig. 4 and its low-frequency spectral index map in Fig. 5. Figure 6 shows an overlay of the ILT radio map on the HST optical continuum image (Pentericci et al. 1999) together with the Lyα contours as observed by the Keck Telescope (Reuland et al. 2003).

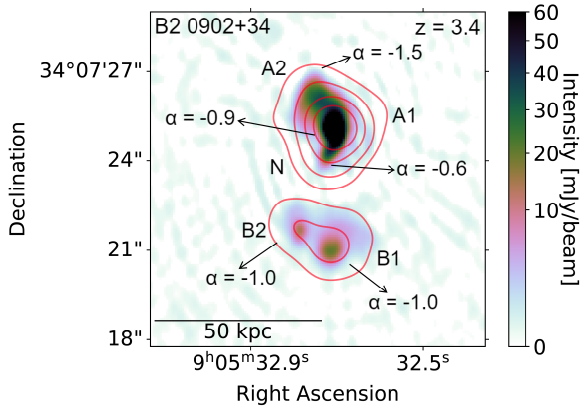

Fig. 4. ILT 144 MHz final processed image of B2 0902+34 at $z = 3.4$, with a resolution of $0.4'' \times 0.2''$ and the VLA contours in the L band.

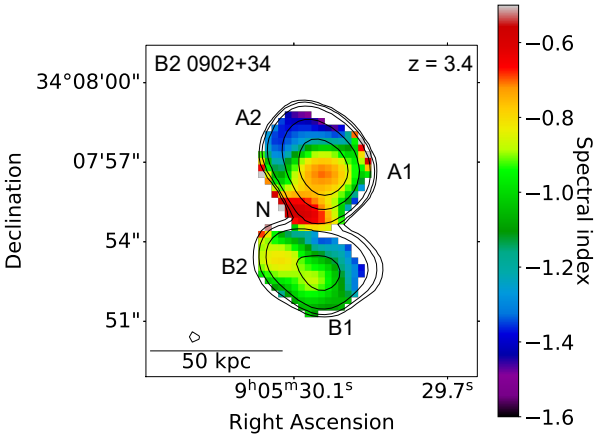

Fig. 5. Map of the low-frequency 144 MHz – 1.4 GHz spectral index of B2 0902+34 at $z = 3.4$, obtained using the ILT HBA and VLA L-band observations. The ILT HBA contours from the smoothed image in Fig. 4 are displayed on the spectral index map.

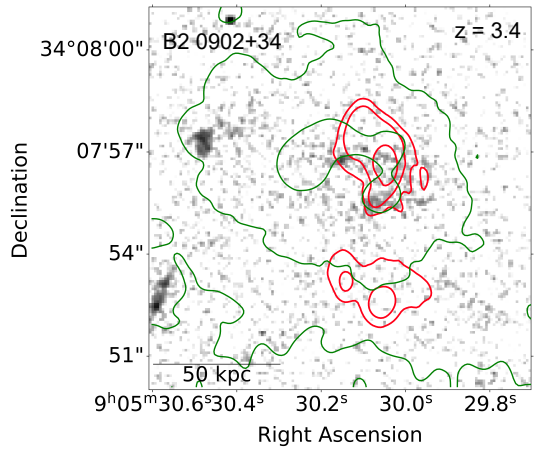

Fig. 6. Overlay of LOFAR ILT radio image for B2 0902+34 at $z = 3.4$ (red contours) superimposed on the HST continuum image (6 h exposure, PC section of WFPC2, $F622W$ filter, Pentericci et al. 1999). The green contours show the Keck Lyα distribution (Reuland et al. 2003).

There are several aspects of the low-frequency radio image and spectral index map of B2 0904+32 that deserve a commentary. The low-frequency ILT image consists of multiple components: the nuclear core N, the northern components A1 and A2,

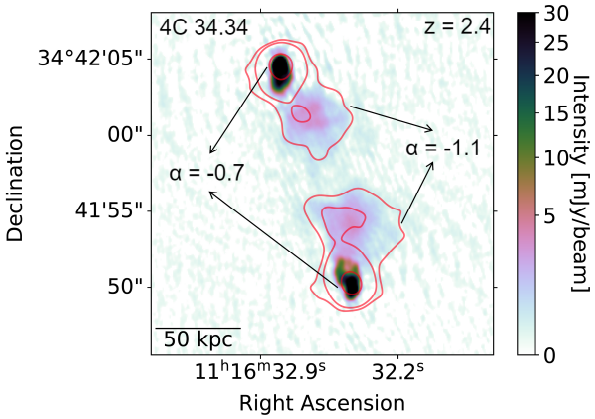

Fig. 7. ILT 144 MHz final processed image of 4C 34.34 at $z = 2.4$, with a resolution of $0.3'' \times 0.2''$ and the VLA contours in the L band.

with an ultra-steep spectrum radio plume having an ultra-steep spectrum with $\alpha = -1.5$ at its northern edge, and a southern lobe with two outer hot spots (B1 and B2; the naming inspired by Carilli 1995). The nuclear core has a spectral index between 1.4 GHz and 144 MHz of $\alpha = -0.60 \pm 0.02$. Although relatively flat, it is steeper than $\alpha = -0.30 \pm 0.02$ measured by Carilli (1995) between 1.65 GHz and 4.70 GHz. It, therefore, appears to have a peaked "GPS-type" spectrum. There is a pair of similar lobes (components B1 and B2) and a highly bright lobe (A1) that extends to the east. Just like for 4C 41.17, the lobes could have appeared from different activity episodes, where the precession of the radio source is jet angle between them (Blundell & Rawlings 1999). However, a more likely explanation for the complex shape of the source is the interaction of the radio jets with the surrounding halo, similarly to the case of 4C 41.17.

B2 0902+34 is located in a protocluster environment (Eales et al. 1993; Pentericci et al. 1999), surrounded by several galaxies. As pointed out by Carilli (1995), B2 0902+34 has an unusual radio structure, with a relatively flat-spectrum core, located in a "valley" between two optical peaks.

The bending of the northern structure eastwards and the southern structure westwards indicates that the jet ejected from the nucleus in the A1-B2 direction is thereafter bent because of its interaction with a rotating gas cloud connected with the Lyα halo visible on the Keck infrared map Lyα map of Reuland et al. (2003) in Fig. 6. The ultra-steep spectrum part of the source (A2) coincides with a region shown by Carilli (1995) to have large rotation measures and gradients in rotation measure that are indicative of a dense, magnetized gas cloud, comparable to those found at the centers of cooling-flow clusters at low redshifts.

4.3. 4C 34.34 at $z = 2.4$

The high-resolution image of 4C 34.34 at 144 MHz is shown in Fig. 7 and the low-frequency spectral index map in Fig. 8. It is not possible to make optical or X-ray overlays similar to those shown for the Anthill in Fig. 3 or B2 0902+34 in Fig. 6 because no comparable non-radio data are available.

We note the following aspects of the low-frequency radio image and spectral index map of 4C 34.34 at $z = 2.4$. The radio structure of 4C 34.34 is typical of high-luminosity FR-II edge-brightened double radio sources, with hot spots at its northern and southern extremities and diffuse emission on both sides extending towards the galaxy nucleus that is not detected by the

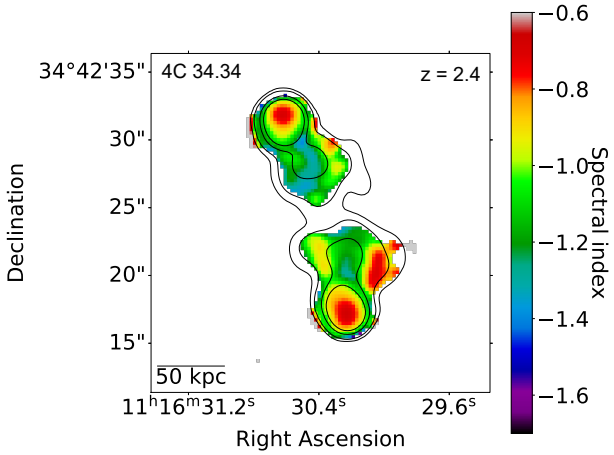

Fig. 8. Map of the spectral index of 4C 34.34 at $z = 2.4$ obtained using the VLA *L*-band and the ILT HBA observations. The ILT HBA contours from the smoothed image in Fig. 7 are displayed on top of the spectral index map.

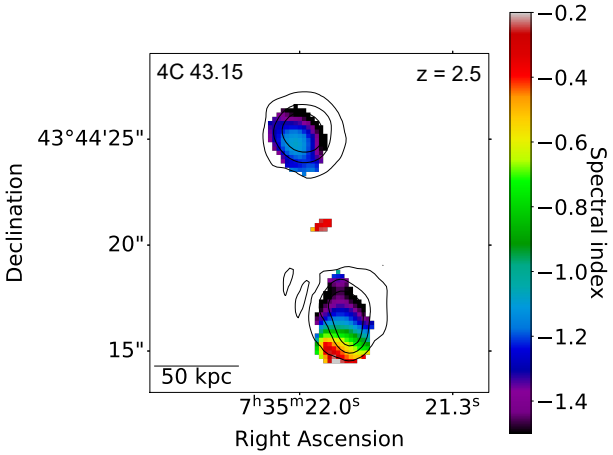

Fig. 10. Map of spectral index of 4C 43.15 at $z = 2.4$ obtained using VLA *X*-band and the ILT HBA observations. The ILT HBA contours from the smoothed image from Fig. 9 are displayed on top of the spectral index map.

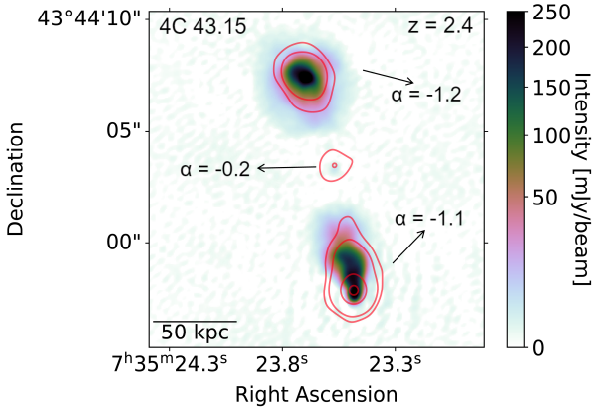

Fig. 9. ILT 144 MHz final processed image of 4C 43.15 at $z = 2.4$, with a resolution of $4'' \times 4''$ and the VLA contours in *X* band.

ILT. The spectral indices of the hot spots are normal for extended radio sources, both with $\alpha = -0.70 \pm 0.04$. The radio "bridge" has an ultra-steep spectrum with $\alpha = -1.10 \pm 0.05$.

4.4. 4C 43.15 at z = 2.4

The high-resolution image of 4C 43.15 at 144 MHz is shown in Fig. 9 and its low-frequency spectral index map in Fig. 10. Both images were taken from Sweijen et al. (2022). Again, no suitable data are available for making optical or X-ray overlays similar to those shown for the Anthill or B2 0902+34.

We note the following aspects of the low-frequency radio image and spectral index map of 4C 43.15 at $z = 2.4$. As with 4C 34.34, the radio structure of 4C 43.15 is typical for a high-luminosity FR-II edge-brightened double radio source, with hot spots at the northern and southern extremities. The spectral indices of the hot spots are normal, both with $\alpha = -0.70 \pm 0.02$ and that of the lobe is steeper, with $\alpha = -1.10 \pm 0.03$. There is a flat-spectrum radio core, bright on the VLA *X*-band image and faint on the ILT HBA image that has a spectral index of $\alpha = -0.40 \pm 0.07$. The similarity between 4C 34.34 and 4C 43.15 is high, both in their radio images and their spectral indices.

A Lyα image (Motohara et al. 2000) and the Lyα, NV, CIV, and HeII spectra (Villar-Martín et al. 2003) show that an ionized gas halo extends asymmetrically to the north and envelopes the northern radio hot spots. The southern hot spot is located outside the ionized gas halo and is more compact than the northern one. This may be because the gas is interacting with and compressing the northern jet during its outward propagation.

5. Discussion

The sub-arcsecond resolution LOFAR images of the four HzRGs discussed above illustrate the diversity of properties exhibited by luminous $z > 2$ radio galaxies and the importance of their study in understanding the role and influence of AGN on the formation and evolution of massive galaxies and galaxy clusters.

5.1. Radio structures as signatures of protoclusters

4C 41.17 (the Anthill) at $z = 3.8$ and B2 0902+34 are both associated with radio structures that appear "bent" or non-linear and are identified with galaxies in dense groups or protoclusters. They are surrounded by giant halos of ionized gas. Their radio structures are non-typical for low-redshift high-luminosity radio sources and have probably been "distorted" by the interaction of their radio jets with the dense protocluster environment at high redshifts. A distorted radio structure has been suggested as a tool for finding protoclusters around high-z quasars by Barthel & Miley (1988).

4C 34.34 at $z = 2.4$ and 4C 43.15 have FR-II edge-brightened structures that are typical for high-luminosity radio sources associated with galaxies and quasars at lower redshift. They do not appear to be located in such dense protocluster environments as 4C 41.17 or B2 0902+34, despite the extended halo of ionized gas that is located asymmetrically with respect to the extended 4C 43.15 radio source.

5.2. Interaction of radio jets with the environment

Radio-optical alignments similar to what is observed for the Anthill (Fig. 3) are seen in many other $z > 3$ HzRGs (Miley & De Breuck 2008) and have been used as evidence that the radio jets in HzRGs can often interact vigorously with the surrounding gas. Several mechanisms have been proposed to explain this interaction, including positive AGN feedback and

jet-cloud deflection. In positive AGN feedback scenarios, the jets induce star formation in the gas as they propagate outwards (Carilli et al. 1997; Pentericci et al. 2000), either by compressing the cold molecular clouds (Silk 2013), or directly in the outflowing gas (Ishibashi & Fabian 2012). Jet-cloud deflection is seen in B2 0902+34 (A2 component) and takes place when the jet hits a highly dense environment, interacts with it, and may be deviated (De Young 1991; Dal Pino 1999). All these mechanisms may be important because they explain the influence of the jets on the interstellar and intergalactic medium around such massive galaxies. Multispectral studies of such interactions from a larger sample of HzRGs are needed to constrain the details of the processes that are occurring.

The Anthill at $z = 3.8$ is one of the most spectacular case study of an emerging dense cluster, similar to but more distant than the Spiderweb at $z = 2.2$. The alignments of the radio emission with the (i) galaxy distribution, (ii) the giant ionized gas halo, and (iii) the X-ray emission indicate the intriguing connection between the various constituents. The additional alignment of the radio jet of the central galaxy (A, B1, C) with the radio jet associated with the possibly merging satellite galaxy B(2+3) is particularly interesting. It is additional evidence that at redshifts $z > 2$ supermassive black holes, massive galaxies, and massive galaxy clusters are built up together in fundamental processes that involve galaxy and SMBH merging and star formation stimulated by the outwardly moving radio-emitting jets.

5.3. Inverse Compton scattering of radio to X-rays

The correspondence of the location and alignment of the radio emission and the X-ray emission in the Anthill is consistent with the X-ray radiation being dominated by inverse Compton up-scattering of the cosmic microwave background photons by the radio-emitting relativistic electrons as also seems to be the case in the Spiderweb protocluster (Carilli et al. 2022; Schwartz 2002; Carilli & Taylor 2002; Scharf et al. 2003). We note that because of the dependence of the energy density of the CMB on $(1 + z)^4$, this would be a factor of ∼5 larger at the redshift of the Anthill than at the redshift of the Spiderweb. However, the ratio of the inverse Compton X-ray emission to synchrotron radio emission is dependent on many unknown factors and assumptions, such as magnetic field strengths and pressures within the radio jets and hot spots (e.g., Carilli et al. 2022; Hodges-Kluck et al. 2021) as well as high spatial resolution at low radio frequencies are important for investigating such processes. The discovery of a luminous radio galaxy with $z = 5.72$ (150 MHz luminosity $10^{29.1}$ W Hz^{-1} and spectral index −1.4 Saxena et al. 2018) implies that IC dimming of radio emission is not substantial for redshifts $z < 6$.

5.4. High-z environment and the α–z relationship

For both the Anthill at $z = 3.8$ and B2 0902+34 at $z = 3.4$, the location of the ultra-steepest part of the radio emission coincides with the Ly α-emitting ionized gas halo. This suggests that the correlation of integrated ultra-steep spectral index with redshift discussed in the introduction may be at least partially due to the location of the synchrotron jets in the dense environment associated with forming protoclusters in the early Universe (Klamer et al. 2006). A statistical comparison of the spatial relationship of radio spectral index with the various resolved constituents of distant radio galaxies will be important in future ILT studies with larger samples.

6. Conclusions and future prospects

This pilot project has shown that sub-arcsecond studies of the low-frequency radio structures of radio galaxies at $z > 2$ with the ILT are feasible and highly informative. Because LOFAR probes the oldest detectable radiating synchrotron electrons and because the extended radio emission contains information about the activity history of the active host nuclei and supermassive black holes, such studies can provide unique information about the formation and evolution of massive galaxies and protoclusters in the early Universe.

We know that HzRGs have several properties that make high-resolution studies with LOFAR uniquely suited to searching for the most distant massive protoclusters and studying how the protocluster AGN and their synchrotron jets interact with the forming parent protoclusters. These include (i) ultra-steep radio spectra that allow LOFAR to detect the oldest detectable radiating synchrotron electrons, (ii) extended radio emission with an angular size distribution well suited to mapping with the international baselines of the ILT (80% between 4 and 20″; e.g., Carilli et al. 1998), and (iii) a structure that is frequently bent or non-linear due to interaction with the extended ionized gas halos that permeate distant radio protoclusters. There are three fundamental diagnostics of HzRGs that require high resolution at low frequencies that are attainable with the ILT.

- Establishing that HzRGs have bent, nonlinear, and asymmetric radio structures can indicate that the associated radio sources are likely to be interacting with a dense protocluster environment. This can pinpoint the location of massive protoclusters and provide important information about their properties (Barthel & Miley 1988; Battye & Browne 2009). It is likely that linear, highly symmetrical sources are located in less dense environments, not specifically to protoclusters.
- Comparisons between spatially resolved low-frequency radio images and high-frequency radio images allows us to calculate the spatially resolved spectral index and, in some cases, (e.g., 4C43.15) to conduct spectral modeling and find out the spectral age of the radio emitting plasma.
- Comparisons of the sub-arcsecond spatial distribution of the radio images and radio spectra with images at non-radio wavebands. These are needed to understand how the forming supermassive black holes and their jets are related to merging, star formation, and other processes involved in building the first massive galaxies and protoclusters.

This pilot project illustrates the potential importance of extreme USS radio sources from the LOFAR-WHT-WEAVE LoTSS surveys (Shimwell et al. 2019) for advancing such studies. Filtered to match the steep spectral indices, angular size distributions, flux ranges, and morphologies of known HzRGs and radio protoclusters, LOFAR samples will enable dense protoclusters such as the Spiderweb and the Anthill to be detected out to the highest redshifts at which they emerged. For example, a radio source with a similar luminosity and spectral index to the Anthill could be detected at high resolution with the ILT to redshifts beyond $z \sim 8$. Hence, samples of USS radio sources from LoTSS form a unique basis for multispectral investigations of interactions between powerful radio jets and the other constituents of protoclusters. Follow-up multispectral studies are likely to provide fundamental information about the simultaneous evolution of massive galaxies, dense protoclusters, and supermassive black holes in the early Universe.

Sub-arcsecond observations of USS radio protoclusters with the ILT would benefit by even higher resolutions than are presently available and such resolutions are feasible. Therefore,

we suggest that extending the ILT baselines by a substantial factor and the addition of ILT stations at strategic locations to achieve more uniform baseline coverage and increased sensitivity should be explored.

Acknowledgements. We thank Chris Carilli for his useful comments. R.J.v.W. and R.T. acknowledge support from the ERC Starting Grant ClusterWeb 804208. This paper is based (in part) on data obtained with the International LOFAR Telescope (ILT). LOFAR (van Haarlem et al. 2013) is the Low Frequency Array designed and constructed by ASTRON. It has observing, data processing, and data storage facilities in several countries, that are owned by various parties (each with their own funding sources), and that are collectively operated by the ILT foundation under a joint scientific policy. The ILT resources have benefitted from the following recent major funding sources: CNRS-INSU, Observatoire de Paris and Université d'Orléans, France; BMBF, MIWF-NRW, MPG, Germany; Science Foundation Ireland (SFI), Department of Business, Enterprise and Innovation (DBEI), Ireland; NWO, The Netherlands; The Science and Technology Facilities Council, UK; Ministry of Science and Higher Education, Poland. The National Radio Astronomy Observatory is a facility of the National Science Foundation operated under cooperative agreement by Associated Universities, Inc. The Jülich LOFAR Long Term Archive and the German LOFAR network are both coordinated and operated by the Jülich Supercomputing Centre (JSC), and computing resources on the supercomputer JUWELS at JSC were provided by the Gauss Centre for Supercomputing e.V. (grant CHTB00) through the John von Neumann Institute for Computing (NIC).

References

Adam, R., Comis, B., Macías-Pérez, J.-F., et al. 2015, A&A, 576, A12
Barthel, P. D., & Miley, G. K. 1988, Nature, 333, 319
Battye, R., & Browne, I. 2009, MNRAS, 399, 1888
Bicknell, G. V., Sutherland, R. S., van Breugel, W. J. M., et al. 2000, ApJ, 540, 678
Blundell, K. M., & Rawlings, S. 1999, Nature, 399, 330
Briggs, D. S. 1995, PhD thesis, New Mexico Institute of Mining Technology, Socorro, New Mexico, USA
Carilli, C. 1995, A&A, 298, 77
Carilli, C., & Taylor, G. 2002, ARA&A, 40, 319
Carilli, C., Owen, F., & Harris, D. 1994, AJ, 107, 480
Carilli, C., Röttgering, H., Van Ojik, R., Miley, G., & Van Breugel, W. 1997, ApJS, 109, 1
Carilli, C. L., Perley, R., Harris, D. E., & Barthel, P. D. 1998, Physics Plasmas, 5, 1981
Carilli, C. L., Anderson, C. S., Tozzi, P., et al. 2022, ApJ, 928, 59
Casey, C., Cooray, A., Capak, P., et al. 2015, ApJ, 808, L33
Chambers, K., Miley, G., & van Breugel, W. 1988, Bull. Am. Astron. Soc., 20, 1027
Chambers, K., Miley, G., & Van Breugel, W. 1990, ApJ, 363, 21
Chandra, P., Swarup, G., Kulkarni, V. K., & Kantharia, N. G. 2004, JApA, 25, 57
da Costa, M. R., & Menéndez-Delmestre, K. 2021, Astron. Nachr., 342, 153
Dal Pino, E. M. D. G. 1999, ApJ, 526, 862
De Gasperin, F., Dijkema, T., Drabent, A., et al. 2019, A&A, 622, A5
Dey, A., van Breugel, W., Vacca, W. D., & Antonucci, R. 1997, ApJ, 490, 698
De Young, D. S. 1989, ApJ, 342, L59
De Young, D. S. 1991, ApJ, 371, 69
Di Mascolo, L., Saro, A., Mroczkowski, T., et al. 2023, Nature, 615, 809
Eales, S., Rawlings, S., Puxley, P., Rocca-Volmerange, B., & Kuntz, K. 1993, Nature, 363, 140
Emonts, B. H., Lehnert, M. D., Yoon, I., et al. 2023, Science, 379, 1323
Fall, S. M., & Rees, M. J. 1977, MNRAS, 181, 37
Greve, T., Stern, D., Ivison, R., et al. 2007, MNRAS, 382, 48
Gurvits, L., Schilizzi, R., Miley, G., et al. 1997, A&A, 318, 11
Hodges-Kluck, E., Gallo, E., Ghisellini, G., et al. 2021, MNRAS, 505, 1543
Intema, H., Jagannathan, P., Mooley, K., & Frail, D. 2017, A&A, 598, A78
Ishibashi, W., & Fabian, A. 2012, MNRAS, 427, 2998
Ivison, R. J., Dunlop, J. S., Smail, I., et al. 2000, ApJ, 542, 27
Jackson, N., Tagore, A., Deller, A., et al. 2016, A&A, 2016, A86
Jackson, N., Badole, S., Morgan, J., et al. 2022, A&A, 658, A2
Jimenez-Gallardo, A., Massaro, F., Paggi, A., et al. 2021, ApJS, 252, 31
Ker, L., Best, P., Rigby, E., Röttgering, H., & Gendre, M. 2012, MNRAS, 420, 2644
Klamer, I. J., Ekers, R. D., Bryant, J. J., et al. 2006, MNRAS, 371, 852
Law-Green, J., Leahy, J., Alexander, P., et al. 1995, MNRAS, 274, 939
Lilly, S. 1988, ApJ, 333, 161
McCarthy, P. J. 1993, ARA&A, 31, 639
McMullin, J. P., Waters, B., Schiebel, D., Young, W., & Golap, G. 2007, CASA Architecture and Applications, 376, 127
Miley, G., & Chambers, K. 1989, European Southern Observatory Conference and Workshop Proceedings, 32, 43
Miley, G., & De Breuck, C. 2008, A&ARv, 15, 67
Miley, G., Chambers, K., Van Breugel, W., & Macchetto, F. 1992, ApJ, 401, L69
Miley, G., Carilli, C., Taylor, G., De Breuck, C., & Cohen, A. 2009, arXiv e-prints [arXiv:0902.3677]
Mohan, N., & Rafferty, D. 2015, Astrophysics Source Code Library [record ascl:1502.007]
Morabito, L. K., & Harwood, J. J. 2018, MNRAS, 480, 2726
Morabito, L. K., Deller, A. T., Röttgering, H., et al. 2016, MNRAS, 461, 2676
Morabito, L., Jackson, N., Mooney, S., et al. 2022, A&A, 658, A1
Motohara, K., Iwamuro, F., Terada, H., et al. 2000, PASJ, 52, 33
Nesvadba, N., Lehnert, M., Eisenhauer, F., et al. 2006, ApJ, 650, 693
Offringa, A. R., & Smirnov, O. 2017, MNRAS, 471, 301
Offringa, A. R., de Bruyn, A. G., Zaroubi, S., et al. 2013, A&A, 549, A11
Offringa, A. R., McKinley, B., Hurley-Walker, N., et al. 2014, MNRAS, 444, 606
Offringa, A. R., Wayth, R. B., Hurley-Walker, N., et al. 2015, PASA, 32, 008
Pentericci, L., Röttgering, H., & Miley, G. 1999, The Most Distant Radio Galaxies, Proceedings of the colloquium, Amsterdam, 15–17 October 1997, Royal Netherlands Academy of Arts and Sciences, eds. H. J. A. Röttgering, P. N. Best, & M. D. Lehnert, 485
Pentericci, L., Van Reeven, W., Carilli, C., Röttgering, H., & Miley, G. 2000, A&AS, 145, 121
Reuland, M., van Breugel, W., Rottgering, H., et al. 2003, ApJ, 592, 755
Ricarte, A., Pacucci, F., Cappelluti, N., & Natarajan, P. 2019, MNRAS, 489, 1006
Saxena, A., Jagannathan, P., Röttgering, H. J. A., et al. 2018, MNRAS, 475, 5041
Saxena, A., Röttgering, H., Duncan, K., et al. 2019, MNRAS, 489, 5053
Scharf, C., Smail, I., Ivison, R., et al. 2003, ApJ, 596, 105
Schwartz, D. A. 2002, ApJ, 571, L71
Shimwell, T., Röttgering, H., Best, P. N., et al. 2017, A&A, 598, A104
Shimwell, T., Tasse, C., Hardcastle, M., et al. 2019, A&A, 622, A1
Silk, J. 2013, ApJ, 772, 112
Sweijen, F., Morabito, L. K., Harwood, J., et al. 2022, A&A, 658, A3
Tielens, A., Miley, G., & Willis, A. 1979, A&AS, 35, 153
Toshikawa, J., Uchiyama, H., Kashikawa, N., et al. 2018, PASJ, 70, S12
Tozzi, P., Pentericci, L., Gilli, R., et al. 2022, A&A, 622, A54
Uchiyama, H., Yamashita, T., Nagao, T., et al. 2022, ApJ, 934, 68
Uson, J. M., Bagri, D. S., & Cornwell, T. J. 1991, Phys. Rev. Lett., 67, 3328
van Haarlem, M. P., Wise, M. W., Gunst, A. W., et al. 2013, A&A, 556, A2
Van Weeren, R., Williams, W., Hardcastle, M., et al. 2016, ApJS, 223, 2
van Weeren, R. J., Shimwell, T. W., Botteon, A., et al. 2021, A&A, 651, A115
Venemans, B., Röttgering, H., Miley, G., et al. 2007, A&A, 461, 823
Villar-Martín, M., Vernet, J., di Serego Alighieri, S., et al. 2003, MNRAS, 346, 273
Williams, W. L., van Weeren, R. J., Röttgering, H. J. A., et al. 2016, MNRAS, 460, 2385
Wylezalek, D., Galametz, A., Stern, D., et al. 2013, ApJ, 769, 79